Improving the Rate Performance of Manganese Dioxide by Doping with Cu^{2+}, Co^{2+} and Ni^{2+} ions

You Yang[1], Xiaobing Huang[2], Yuqing Yang[1], Cailin Wu[1], Ben Lei[1], Qirong Peng[1], Guoping Wang[1,*]

[1] College of Chemical Engineering, University of South China, Hengyang 421001, China
[2] College of Chemistry and Chemical Engineering, Hunan University of Arts and Science, Changde 415000, China
[*]E-mail: wgpcd@aliyun.com

Metal-doped MnO_2 has been successfully synthesized via chemical precipitation method. Interestingly, doping can increase not only ion conductivity but also intrinsic electron conductivity. By doping, the particle size of MnO_2 decreases, relatively appropriate pore size distribution is obtained, and physically and chemically bound water content increases, all of which contribute to ion conductivity. Meanwhile, doping has induced some defects in MnO_2 crystal, increasing the hole concentration and then intrinsic electron conductivity. As the result, metal–doped MnO_2 displays better rate performance than the un–doped. Especially, nickel–doped MnO_2 exhibits the best rate behavior. Even at 8 A g^{-1}, nickel–doped MnO_2 still has a specific capacitance as high as 234.0 F g^{-1}, larger than that of the un–doped obtained at 1 A g^{-1} (only 173.6 F g^{-1}). In conclusion, doping is a useful way for improving the rate performance of MnO_2.

1. INTRODUCTION

Serving as one kind of supercapacitor electrode materials, transition metal oxides can store energy not only through ion adsorption/desorption within electrochemical double-layer but also through fast and reversible redox reactions on the surface of electrode materials. As the result, they can provide a specific capacitance as much as 10-100 times higher than that of electronic double-layer capacitor electrode materials, and more and more researchers are focusing on this kind of material.

Among the transition metal oxides, ruthenium oxide has been extensively studied because of its exceptional properties such as metallic-type conductivity, good thermal stability, high specific energy and high rate performance [1]. However, its large commercialization has been blocked by its high cost,

high toxicity and low reserves. A significant effort has been put into finding cheaper and environmentally friendly materials. Since Lee and Groodenough [2] reported the electrochemical properties of manganese dioxide in 1999. Researchers are turning their attention to MnO_2 electrode material owing to its abundance in nature, low price, environmental friendliness and high theoretical specific capacity (1370 F g^{-1} within the potential window of 0-0.8 V). Relative study on manganese oxide has extended from one-dimensional to three-dimensional nanostructure[3-6] and it has been considered as an alternative candidate electrode material for electrochemical supercapacitor. Unfortunately, MnO_2 usually suffers from low electrical and ion conductivity [7]. As the result, its specific capacitance often decreases dramatically with increasing the thickness of the electrode and potential scan rate, and the rate capability is far from the need of large power for supercapacitor. In attempt to promote its electrical conductivity, highly conductive additives are often introduced into the composite electrode. The common conductive additives involve active carbon [8], carbon nanotubes fibers [9], carbon nanotube (CNT) [10], graphene [11], polyaniline [12], polypyrrole[13], polythiophene [14]. For example, the composite of Mn oxide/CNT [15] could reach a specific capacitance of 415 F g^{-1}, because CNTs provided electronic conductive paths and formed a network of open mesopores. Without any doubt, the presence of conductive additives can form a three-dimensional conducting network and significantly improve the apparent electron conductivity of MnO_2 electrode. Nevertheless, with regard to its poor intrinsic electron conductivity and ion conductivity, it is beyond the reach of conductive additives. Consequently, the rate performance, which is a critical performance for supercapacitor, is still not satisfied. To achieve higher rate performance, it is necessary to further improve its intrinsic electron conductivity and ion conductivity.

Electrical properties are determined by crystal structure and the defect. It has been reported that the electrical conductivity of electrical insulator can be dramatically improved by changing stoichiometry or introducing dopants [16]. Through accommodating foreign substitutional ions with various valence and ionic radii, defects has been introduced into the crystal lattice, altering the conductivity by contributing electron or hole. For instance, defect cation can result in electron hole, increasing the valence state of corresponding positive ion and in turn the conductivity of the crystal. Doping technology has been widely applied to semiconductor field for optimizing their electrical properties. Bismuth [17], silver [18], iron [19] and cobalt [20] have been successfully doped into titanium oxide and cerium gadolinium oxide to change the density of electron states in the band gap of the semiconductor structure, giving rise to higher intrinsic conductivity of crystal. Only 0.05% Bi^{3+} can lead to a 2.67-fold increase in the conductivity of TiO_2 [17]. Generally, the doping effect may be much better if the radius of doping ion is closer to the radius of the metal ion substituted. Thus, here we chosen Cu^{2+} (0.073 nm), Co^{2+} (0.065 nm) and Ni^{2+} (0.069 nm) as the dopants for MnO_2 because of their similar radius to Mn^{4+} (0.065nm).

In this paper, manganese oxide was doped successfully with Cu^{2+}, Co^{2+}, Ni^{2+} and their effects on the electrochemical properties have been investigated by cyclic voltammetry (CV), galvanostatic charge-discharge (GCD) and electrochemical impedance spectra (EIS) in 0.5mol L^{-1} Na_2SO_4 solution. The results demonstrate that metal doping can improve not only the ion conductivity but also the intrinsic electron conductivity of MnO_2 and then the rate capability. Especially, in the presence of nickel, MnO_2 are expected to show much better rate capability.

2. EXPERIMENT SECTION

2.1. Material synthesis

Manganese dioxide was doped by facile chemical precipitation method. The synthesis process typically involves three steps: (1) 3 mmol manganese sulfate monohydrate and 0.45 mmol nickel nitrate hexahydrate were dissolved in 40 ml deionized water, and then 4 mmol potassium permanganate was slowly added into the above mixture solution. (2) The reaction lasted for 12 hrs at room temperature. (3) After filtered, the precipitation was washed with deionized water for several times. The samples obtained were dried at 80°C for 8 hrs. The product prepared was marked as MnO_2-Ni. Such a process was also adopted to prepare the un-doped, cobalt-doped and copper-doped manganese dioxide, which were marked as MnO_2-undoped, MnO_2-Co, MnO_2-Cu, respectively.

2.2 Materials characterization

The crystal structures of manganese dioxide were characterized using MAX2200 X-ray diffractometer. The scanning wavelength was 0.02° and the diffraction angle ranged from 5 to 90°. It was operated at 40 kv using Cu Kα radiation at a scanning rate of 5° min^{-1}. The morphologies and sizes of the as-prepared samples were observed using scanning electron microscopy (SEM, Zeiss Super55 operated at 5kV). The specific surface areas of the materials were tested by Beijing 3H-2000PS2 volumetric adsorption analyzer utilizing nitrogen as adsorption/desorption gas at 77.3 K, and the corresponding values were determined according to brunnauer emmett teller (BET) method. The pore size distribution was analyzed with the Barrett-Jouner-Halenda (BJH) method. Fourier transform infrared spectrometer (FT-IR) were obtained with Bruker Prestige-21 by dispersing the sample in KBr and pressing it into transparent pellets. The surface element analysis of the samples were performed by energy dispersive X-ray spectrometry (EDS, Oxford X-Max 20).

2.3 Preparation of electrodes and electrochemical characterization

The electrochemical performance was evaluated using CH660E electrochemical working station with a three-electrode system. Platinum electrode served as the counter electrode, saturated calomel electrode as the reference electrode and glassy carbon electrode as the working electrode. The working electrode was prepared as follows: Firstly, under ultrasonication, carbon nanotubes (1.5 mg) and manganese oxide (9.0 mg) were dispersed in 5.0 ml isopropanol for 30 min to form a homogeneous solution. Then, 5.0 µL of the above homogeneous solution was pipetted gradually onto the surface of a glassy carbon electrode. After naturally drying, the surface of glass carbon electrode was covered with 5 µL of the dilated Nafion® solution (0.1% wt%, Aldrich) to form a uniform electrode protection layer. The samples' electrochemical performances were characterized by CV within a potential window ranging from 0 to 0.8 V at 5 mV s^{-1} potential scanning rate. The GCD curves were measured at the scale ranging from 1 to 8 A g^{-1}. The EIS was measured within a frequency range of 1~100000 Hz. The electrolyte solution used in the electrochemical performance test experiments was 0.5 mol L^{-1} Na_2SO_4

solution. The specific capacitance of the electrode materials was estimated from the charge-discharge curves according to the equation:

$$C_{sp} = \frac{I \times \Delta t}{\Delta V \times m}$$

where C_{sp} was the specific capacitance, I was the charge-discharge current (A), Δt was the discharge time (s), ΔV was the charge-discharge potential window (V), and m was the mass of the active material (g).

3. RESULTS AND DISCUSSION

Fig. 1 depicts the XRD patterns of the metal ion-doped and un-doped birnessite manganese dioxide. No sharp diffraction peaks appear in the four samples, suggesting their poorly crystallized structure. Meanwhile, all the XRD patterns have two identical broader diffraction peaks at 37.3° and 66.2°, which are well indexed to (1, 1, 1) and (0, 0, 5) planes of JCPDS No.80-1098, respectively. This indicates that the samples can be categorized into birnessite manganese dioxide, agreeing well with the manganese dioxide obtained by Kim [26]. In addition, compared with undoped MnO_2, the three doped oxides show no obvious impurity peaks, implying the forming of solid solution in the doped samples.
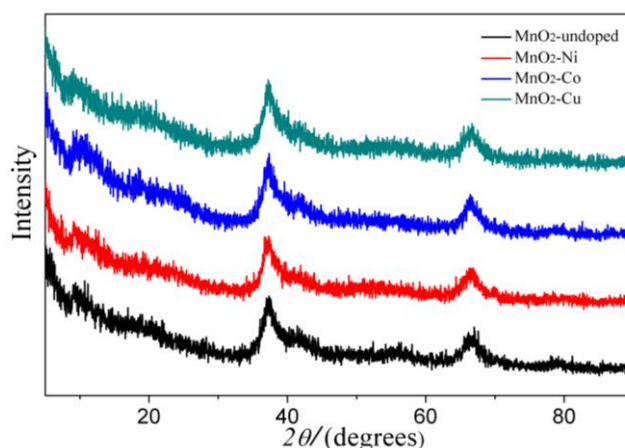
Figure 1. XRD patterns of MnO_2-undoped, MnO_2-Ni, MnO_2-Co and MnO_2-Cu

Fig. 2 shows the SEM images of the four manganese dioxides. It can be seen that the four samples show similar morphology. Nevertheless, the undoped MnO_2 shows an average particle size of about 400 nm, much larger than that of doped MnO_2. Particularly, MnO_2 doped with Ni^{2+} or Co^{2+} presents an average particle size no more than 200 nm, only about one half of the un-doped MnO_2. Based on the phenomenon, it can be concluded that doping agents may decrease the surface energy of MnO_2 seeds and preventing the seed from further growing [32]. In other references, similar effect on morphology and particle size of oxides has been reported for ion doping [27,33], but the variation of the material particles after doping is more obvious in this paper.
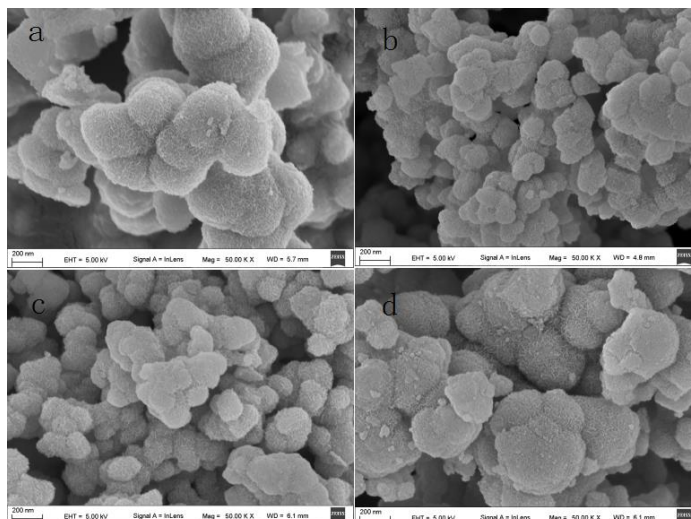
Figure 2. SEM images of MnO$_2$-undoped, MnO$_2$-Ni, MnO$_2$-Co and MnO$_2$-Cu

EDS was used to identify the element composition of the composite. As shown in Fig. 3, four samples show the presence of potassium ions. It has been reported that potassium ions may enter manganese vacancies of manganese oxygen octahedral to make the crystal more stable [21]. Meanwhile, the peaks of nickel, cobalt and copper are observed in the corresponding samples, indicating that nickel, cobalt and copper ions may have entered into manganese dioxide crystal lattice. According to the collected data from Fig. 3, the rate of X/Mn (X=Ni,Co,Cu) is determined to be 0.0176, 0.0459 and 0.0341, respectively.
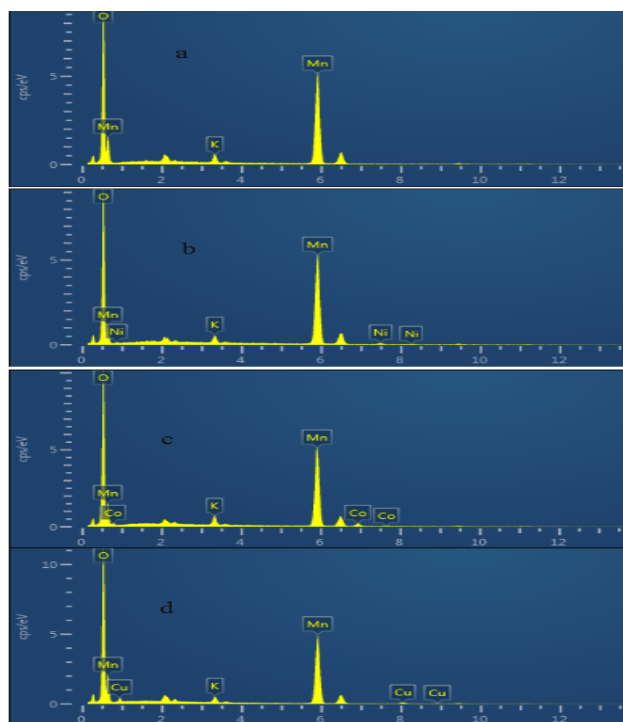
Figure 3. The EDS analysis image of (a) MnO$_2$-undoped, (b) MnO$_2$-Ni, (c) MnO$_2$-Co and (d) MnO$_2$-Cu

The specific surface was determined by Brunauer-Emmett-Teller using nitrogen as adsorption gas at 77.3 K. As shown in Fig. 4a, at very low partial pressure, all the four isotherms increase abruptly. Especially, for Ni^{2+}-doped MnO_2, its micropore volume can be as four times as that of the un-doped, implying its largest volume of micropores. With the increase of partial pressure ($P/P_0>0.45$), the metal-doped MnO_2 displays some hysteresis in the adsorption isotherms, indicating the existence of mainly mesopores (>2.0 nm) in those samples [39]. Among them, Ni^{2+}-doped MnO_2 shows more pronounced hysteresis, indicating its larger amount of mesopores. However, in the MnO_2-undoped, there is almost no hysteresis. This suggests that the amount of mesopores in it is very small. When the partial pressure approximates to unity, no plateau (namely, saturation) is observed in all the four samples because of the multilayer formation. This observation provides the evidence for the presence of macropore, which originates from the large aggregates of particles. Here, it must be pointed out that the rise in the isotherm of MnO_2-Co is the steepest, which suggests the highest volume of macropores. The above results agree well with the BJH pore-size distribution. From Fig. 4b, it can be seen that metal–doping has led to some more micro– and meso–pore volume. Among them, MnO_2-Ni shows the largest micropore and mesopore volume than the others, particularly at the pore diameter of about 3.9 nm. These results may account for the highest specific surface area of MnO_2-Ni. Its calculated specific surface area reaches as high as 140.7 $m^2 \, g^{-1}$, much higher than that of MnO_2-Co (67.2 $m^2 \, g^{-1}$), MnO_2-Cu (68.1 $m^2 \, g^{-1}$) and the MnO_2-undoped (only 35.0 $m^2 \, g^{-1}$). Compared with the undoped manganese dioxides (15-68 $m^2 \, g^{-1}$) prepared by Nayak [34], our doped manganese dioxides show much larger specific surface area. The average pore sizes calculated by BJH mode from the pore size distribution are 5.1, 5.8, 11.8 and 7.1 nm for MnO_2-undoped, MnO_2-Ni, MnO_2-Co and MnO_2-Cu, respectively.
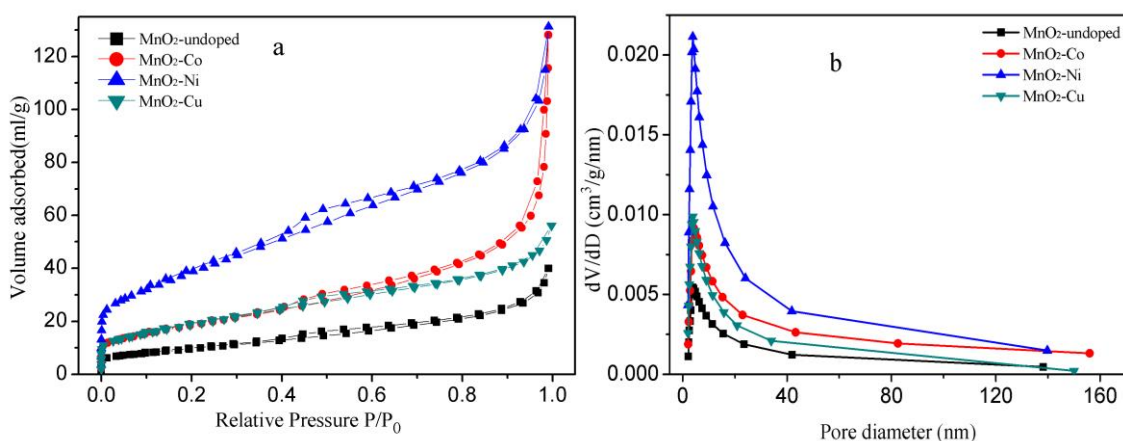
Figure 4. (a) The nitrogen adsorption-desorption isotherms; (b) the pore-size distribution of MnO_2-undoped, MnO_2-Ni, MnO_2-Co and MnO_2-Cu

The FT-IR spectra of MnO_2-undoped, MnO_2-Ni, MnO_2-Co and MnO_2-Cu are presented in Fig. 5. The absorption bands at around 3390 and 1629 cm^{-1} correspond to O-H stretching vibration absorption and bending vibrations absorption of water, respectively. According to Lambert-Beer law, the stronger the absorbance is, the higher the corresponding component concentration. Apparently, the above two peaks in the doped MnO_2 are much stronger than in the MnO_2-undoped. This phenomenon points to the

fact that water content in the doped MnO_2 is higher. This may be because the doping metal ions make MnO_2 easily form hydrates [22]. Simliarly, Chen [35] has reported that iron doping can results in higher content of crystal water, which is line with our results. In addition, all the samples show a strong characteristic peak at around 534 cm^{-1}, which can be assigned to Mn-O stretching vibrations [36]. However, the characteristic peaks of nickel, cobalt and copper oxides are not obvious in the corresponding compound except that the peak at about 534 cm^{-1} extends to some larger wavenumber. Two factors may contribute to such a result. One is the amount of doping elements is in trace. The other is that doping elements can substitute for manganese in the crystal due to their similar size and their characteristic peak are very close to that of manganese oxide. Thus, they overlaid to form broad peaks.
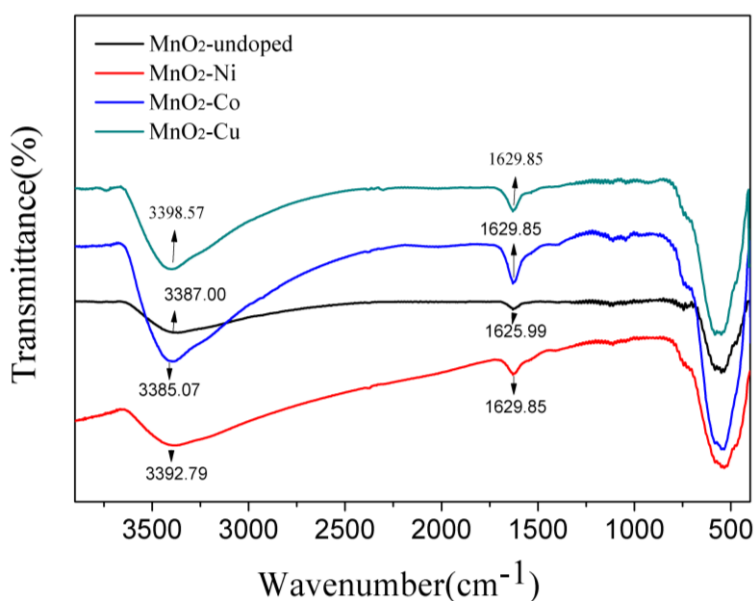
Figure 5. The FT-IR patterns of MnO_2-undoped, MnO_2-Ni, MnO_2-Co and MnO_2-Cu

The electrochemical properties were investigated by CV, GCD and EIS. Fig. 6a displays the typical CV curves of the four samples at 5 mv s^{-1}. The curves of MnO_2-undoped and MnO_2-Ni are quasi-rectangular and symmetrical, indicating their ideal electrical double-layer capacitive behavior. Generally, metal–doped MnO_2 shows larger integrated area than the MnO_2-undoped, implying their larger specific capacitance. This may be attributed to their higher specific surface, which can expose more electrochemical active points for the storage of electrostatic charge at the double-layer interface. These consistent with the charge/discharge curves presented in Fig. 6b. In this figure, MnO_2-undoped and MnO_2-Ni show a charge/discharge profile with quasi–triangular mirror-like symmetrical distribution, suggesting they store charges mainly in an electrochemical double-layer. Meanwhile, metal–doped MnO_2 spends longer charging–discharging time than the un-doped. It is worthy to note that the profiles of MnO_2-Co and MnO_2-Cu deviate far from triangle and their charging time is much longer than their discharging time. From these, it can be concluded that some irreversible processes may take place in MnO_2-Co and MnO_2-Cu. Based on GCD curves, the discharge specific capacitances of MnO_2-undoped, MnO_2-Ni, MnO_2-Co and MnO_2-Cu are calculated as 172.6, 335.1, 412.3 and 435.5 F g^{-1} at 1 A g^{-1}, respectively.

　　　　Whether or not MnO_2 is doped, the discharge specific capacitance decreases with the increase of current density (Fig. 6c). However, metal–doped MnO_2 presents much larger specific capacitance than the un–doped no matter what the current density is. Even at 8 A g^{-1}, their specific capacitance is still larger than that of the un–doped obtained at 1 A g^{-1}. Particularly, Ni–doped MnO_2 exhibits the best rate performance. At the current density of 8 A g^{-1}, its discharge specific capacitance can reach 234.0 F g^{-1}, maintaining about 70% of its specific capacitance obtained at 1 A g^{-1}.

　　　　Table 1 compares the obtained electrochemical performance of our MnO_2-based materials with those results reported in references. Although some results are very close to reference, the experiment conditions are quite different. Since this paper focuses on the rate performance, the scan rate or current density generally is higher than those of most references, and some higher specific capacitance has been achieved compared with those results in references [24-27]. Although sodium-doped manganese oxide has a rate performance of 75.4% (at scan rate of 10 mv s^{-1} compared with the specific capacitance at a scan rate of 1 mv s^{-1}). This improved performances originate with hierarchical pore structure and amorphous structure [40].

Table 1. Comparison of Cs with other MnO_2-based electrodes

Electrode Materials	Cs (F/g)	Scan rate or current density	Electrolyte	References
MnO_2-B	269.0 F/g	50 mV S^{-1}	0.5M Na_2SO_4	24
MnO_2-Ag	770 F/g	2 mV S^{-1}	0.5M Na_2SO_4	25
MnO_2-Co	415 F/g	0.2 A g^{-1}	1M Na_2SO_4	26
MnO_2-Al	64.3 F/g	2 mV S^{-1}	0.1M Na_2SO_4	27
MnO_2/AC	375 F/g	0.1 A g^{-1}	1M Na_2SO_4	28
MnO_2/CNF	238 F/g	0.1 A g^{-1}	1M Na_2SO_4	28
MnO_2/CNT	349 F/g	0.1 A g^{-1}	1M Na_2SO_4	28
Sn@rGo-MnO_2	460.9 F/g	20 mV S^{-1}	1M Na_2SO_4	11
La-MnO_2(1:9)/MWCNTS	130 F/g	2 mV S^{-1}	0.1M Na_2SO_4	29
MnO_2/MWNT	285.1 F/g	1.0 A g^{-1}	1M Na_2SO_4	30
MnO_2/NG	302 F/g	1.0 A g^{-1}	1M Na_2SO_4	31
MnO_2-Ni	335.1 F/g	1.0 A g^{-1}	0.5M Na_2SO_4	This work
MnO_2-Co	412.3 F/g	1.0 A g^{-1}	0.5M Na_2SO_4	This work
MnO_2-Cu	435.5 F/g	1.0 A g^{-1}	0.5M Na_2SO_4	This work

ABBREVIATIONS:

Sn@rGo-MnO_2: Sn doped reduced graphene oxide/manganese dioxide nanocomposites, La-MnO_2 (1:9)/MWCNTS: Lanthanum doped manganese dioxide/carbon nanotube composites, MnO_2/AC: activated carbor doped manganese dioxide, MnO_2/CNF:carbon nanofiber doped manganese dioxide, MnO_2/CNT:carbon nanotube doped manganese dioxide, MnO_2/MWNT: MnO_2 nanoparticles adhered on multi-walled carbon nanotubes, MnO_2/NG: manganese dioxide/Nitrogen-doped graphen composites.

The reasons for the better rate performance of metal–doped MnO_2 may involve: (1) Appropriate pore size distribution and particle size. Metal–doping has resulted in more micro– and meso–pore, especially MnO_2-Ni possesses the most micropore and mesopores. Large amount of micropores can dramatically improve specific surface area and then expose more active sites, increasing the specific capacitance [37]. Appropriate mesopores can facilitate the storage and transportation of electrolyte within electrode material, making electrolyte's entry into the pores easy and decreasing ion diffusion resistance and increasing the rate performance.
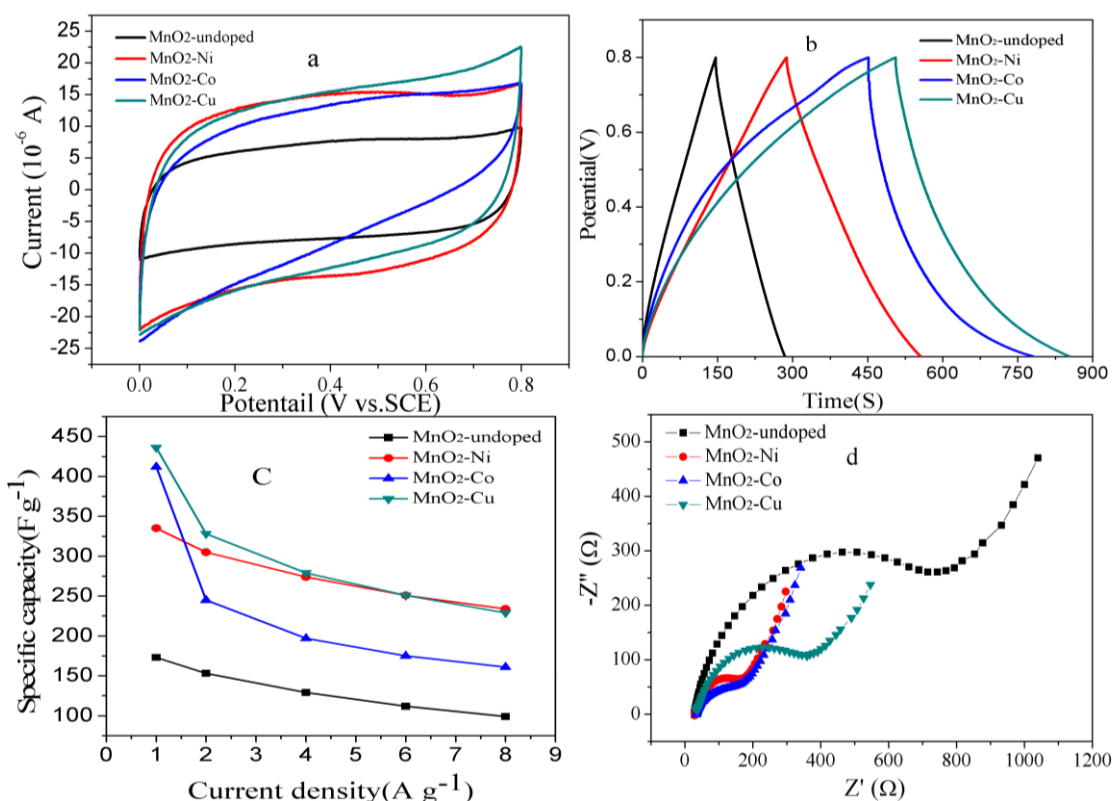
Figure 6. (a) CV curves of MnO_2-undoped, MnO_2-Ni, MnO_2-Co and MnO_2-Cu at a scan rate of 5mV s^{-1}. (b) GCD of MnO_2-undoped, MnO_2-Ni, MnO_2-Co and MnO_2-Cu at current density of 1 A g^{-1}. (c) Corresponding specific capacitance at different current density. (d) EIS of MnO_2-undoped, MnO_2-Ni,MnO_2-Co and MnO_2-Cu

Besides, for metal–doped MnO_2, their smaller particle size can also shorten the transportation distance of ions and decrease ion diffusion resistance [38]. (2) Higher water content. It is believed that physically and chemically bound water is expected to improve the transportation of electrolyte ions inside the electrode layer [23]. Therefore, the higher water content in metal–doped MnO_2 may result in better ion conductivity. Fast ionic conduction can weaken polarization of the electrode and then heighten rate performance. The EIS plots have further offered the convinced evidence for the higher ionic conductivity of metal–doped MnO_2. As shown in Fig. 6d, all the slopes of their straight lines at low frequency region are higher than that of the MnO_2-undoped. The higher the slope of straight line is, the higher the diffusion rate of electrolyte ions. (3) Higher electron conductivity. The semicircle of EIS plot at high frequency region represents the resistance of charge transfer in material. Smaller semicircle

diameter indicates the charge-transfer resistance is lower. From Fig. 6d, it can be seen that metal–doped MnO_2 has a smaller semicircle in the high frequency region, suggesting their higher electron conductivity. The calculated charge-transfer resistances are 687.5, 133.4, 145.7, 191.0 Ω for MnO_2-undoped, MnO_2-Ni, MnO_2-Co and MnO_2-Cu, respectively. The decrease in charge-transfer resistances of metal–doped MnO_2 may originate from the increase of hole concentration. Since the valence state of doping metal ion is lower than that of manganese ion, the doping may induce vacancies in the cation, that is, surplus negative ions in the crystal. To keep the electron neutrality in the substitutional sites, some of the metal cations are oxidized to higher valence state. Similar to doping metal in cerium gadolinium oxide [20], Co/Ni may present in a mixing state of Co^{2+}/Co^{3+} or Ni^{2+}/Ni^{3+}, and parts of Mn^{4+} are oxidized to higher valence state in MnO_2-Cu crystal, resulting in a contribution to electronic conduction. On the basis of the above described, doping may create traps for holes of MnO_2 and increases the hole concentration, giving rise to higher conductivity.

4. CONCLUSIONS

Metal-doped MnO_2 has been successfully synthesized and their electrochemical properties have been investigated. Although doping doesn't influence the crystal structure, it can prevent the seed from further growing, resulting in small particle size. Meanwhile, more micro–pores, meso–pores and specific surface area are found in metal–doped MnO_2, especially in MnO_2-Ni. In addition, metal–doped MnO_2 contains larger amount of water than the MnO_2-undoped. Their small particle size, appropriate pore size distribution and higher water content can lead to better ion conductivity. These are all beneficial for improving rate performance. Moreover, doping has induced some defects in crystal. Because of the defects, some metal ions exist in a mixing valence state in the crystal, and the hole concentration increases. As the result, metal–doped MnO_2 displays much larger rate specific capacitance than the MnO_2-undoped. Especially, nickel–doped MnO_2 exhibits the best rate capacity. Even at 8 A g^{-1}, MnO_2-Ni still shows much larger specific capacitance than that of the MnO_2-undoped obtained at 1 A g^{-1}. In conclusion, doping is a useful way for improving the ion and electron conductivity of MnO_2, and then the rate performance.

References

1. X.M. Shi , W.P. Zhou, D.L. Ma, Q. Ma, D. Bridges, Y. Ma and A.M. Hu, *J. Nanomater.*, 16 (2015) 122.
2. H.Y. Lee and J.B. Goodenough, *J. Solid State Chem.*, 144 (1999) 220.
3. C.S. Johnson, *J. Power Sources*, 165 (2007) 559.
4. N. Wang, L. Guo, L. He, X. Cao, C.P. Chen, R.M. Wang and S.H Yang, *Comm.*, 3 (2007) 606.
5. G.Y. Zhao, C.L. Xu and H.L. Li, *J. Power Sources*, 163 (2007) 1132.

6. T.D. Xiao, P.R. Strutt, M. Benaisd, H. Chen and B.H. Kear, *Nanostruct. Mater.*, 10 (1998) 1051.
7. V. Augustyn, P. Simon and B. Dunn, *Energ. Environ. Sci.*, 7 (2014) 1597.
8. M. Yao, X. Zhao, L. Jin, F. Zhao, J. Zhang, J. Dong and Q. Zhang, *Chem. Eng. J.*, 322 (2017) 582.
9. A. Pendashteh, E. Senokos, J. Palma, M. Andersona, J.J. Vilatelac and R. Marcilla, *J. Power Sources*, 372 (2017) 64.
10. H. Zhang, G. Cao, Z. Wang, Y. Yang, Z. Shi and Z. Gu, *Nano Lett.*, 8 (2008) 2664.
11. D. Shanbhag, K. Bindu, A.R. Aarathy, M. Ramesh, M. Sreejesh and H.S. Nagaraja, *Mater. Today Energy*, 4 (2017) 66.
12. G. Han, Y. Liu, L. Zhang, E. Kan, S. Zhang, J. Tang and W. Tang, *Sci. Rep.*, 4 (2014) 4824.
13. W. He, C. Wang, F. Zhuge, X. Deng, X. Xu and T. Zhai, *Nano Energy*, 35 (2017) 242.
14. R. Liu and S.B. Sang, *J. Am. Chem. Soc.*, 130 (2008) 2942.
15. C.Y. Lee, H.M. Tsai, H.J. Chuang, S.Y. Li, P. Lin and T.Y. Tseng, *J. Electrochem. Soc.*, 152 (2005) A716.
16. T. Shi, Y. Chen and X. Guo, *Prog. Mater. Sci.*, 80 (2016) 77.
17. C.J. Cerrilloa, A.N.C. Mendozaa, R.P.M. Romeroa, G.A. Hernandez and H. Hu, *Mater. Sci. Semicond. Process*, 72 (2017) 106.
18. H.J. Vargas, S. Coste, M.A. Garcia, F.R. Carrillo and A. Kassiba, *J. Alloys Compd.*, 710 (2017) 355.
19. H.N. Yoo, D.H. Park and S.J. Hwang, *J. Power Sources*, 185 (2008) 1374.
20. S. Taub, K. Neuhaus, H.D. Wiemhöfer, N. Ni, J.A. Kilner and A. Atkinson, *Solid State Ionics*, 282 (2015) 54.
21. Y. Liu, Y. Qiao, W. Zhang, H. Wang, K. Chen, H. Zhu, Z. Li and Y. Huang, *J. Mater. Chem. A*, 3 (2015) 7780.
22. J. Kang, A. Hirata, L. Kang, X. Zhang, Y. Hou, L. Chen, C. Li, T. Fujita, K. Akagi and M. Chen, *Angew. Chem. Int. Ed.*, 52 (2013) 1664.
23. G. Wang, L. Zhang, J. Zhang, *Chem. Soc. Rev.*, 43 (2012) 797.
24. H. Chi, Y. Li, Y. Xin and H. Qin, *Chem. Commun.*, 50 (2014) 13349.
25. Y. Wang and I. Zhitomirsky, *Mater. Lett.*, 65 (2011) 1759.
26. B. Kim, C. Raj, W. Cho, W. Lee, H. Jeong and K. Yu, *J. Alloys Compd.*, 617 (2014) 491.
27. Y. Li and H. Xie, *Ionics*, 16 (2010) 21.
28. Y. Zhang, Q. Yao, H. Gao, L. Wang, X. Jia, A. Zhang, Y. Song, T. Xia and H. Dong, *Powder Technol.*, 262 (2014) 150.
29. R. Xue, Yan, W. Yan, Y. Tian and L. Yi, *Acta. Phy. Chim. Sin.*, 27 (2011) 2340.
30. Y. Qian, C. Huang, R. Chen, S. Dai and C. Wang, *Int. J. Electrochem. Sci.*, 11 (2016) 7453.
31. B. Huang, C. Huang and Y. Qian, *Int. J. Electrochem. Sci.*, 12 (2017) 11171.
32. J. Wang, N. Zhao, B. Fang, H. Li, T. Bi and J. Wang, *Chem. Rev.*, 115 (2015) 3433.
33. Y. Liu, Y. Qiao, W. Zhang, H. Wang, K. Chen, H. Zhu, Z. Lia and Y.H. Huang, *J. Mater. Chem. A*, 3 (2015) 7780.
34. P. Nayak, T. Penki and N. Munichandraiah, *J. Electroanal Chem.*, 703 (2013) 126.
35. N. Yoo, D. Park and S. Hwang, *J. Power Sources*, 185.2 (2008) 1374.
36. Q. Liu, M. Wang, Y. Wu, K. Fan and Q. Zhang, *J. Funct. Mater.*, 36 (2005) 404.
37. K. Sakaushi, Y. Oaki, H. Uchiyama, E. Hosono, H. Zhou and H. Imai, *Small*, 6 (2010) 776.
38. W. Wang, Y. Sun, B. Liu, S. Wang and M. Cao, *Carbon*, 91 (2015) 56.
39. A. Ide, R. Voss, G. Scholz, G.A. Ozin, M. Antonietti and A. Thomas, *Chem. Mater.*, 19 (2007) 2649.
40. Q. Ma, M. Yang, X.H. Xia, H. Chen, L. Yang and H.B. Liu, *Electrochim. Acta*, 291 (2018) 9.